Optik 157 (2018) 1027–1034

Contents lists available at ScienceDirect

Optik

journal homepage: www.elsevier.de/ijleo

Original research article

Defringing in interference imaging spectrometer based on BEMD and PCA

Wenyi Ren[a], Dan Wu[b], Guoan Yang[c], Jiangang Jiang[a,*], Yingge Xie[a], Guangyuan Du[a], Guodong Wang[a], Sheqi Zhang[a]

[a] School of Science, Northwest A&F University, Yangling 712100, China
[b] College of Mechanical and Electronic Engineering, Northwest A&F University, Yangling 712100, China
[c] School of Electronic and Information Engineering, Xi'an Jiaotong University, Xi'an 710049, China

ARTICLE INFO

Article history:
Received 7 June 2017
Accepted 22 November 2017

Keywords:
Interference imaging spectrometer
Fringe analysis
Empirical mode decomposition
Nonlinear signal processing

ABSTRACT

The constructive and destructive fringe due to etaloning effects is an universal phenomenon emerging in the imaging system using the back-illuminated CCD. An adaptive method based on the bi-dimensional empirical mode decomposition (BEMD) and principal component analysis (PCA) was proposed to suppress the nonlinear fringe in interference imaging spectrometer. The feasibility was verified by reconstructing the fringe and interferogram taken by interference imaging spectrometer effectively. Meanwhile, the vertical CCD mosaic stripes was suppressed obviously. Comparing the retrieved contaminated and corrected spectrums, it was found that the sidelobes introduced by the nonlinear background was removed. It provides us a time-saving, without prior knowledge, and automatic approach for defringing.

1. Introduction

Optical etaloning, caused by interference with wavelengths in the visible to near-infrared (NIR) spectral region, is an issue on the back-illuminated back-thinned CCD which exhibits increased sensitivity and quantum efficiency because incident photons interact directly with the photosensitive silicon substrate without having to penetrate an electrode layer (as is the case of a front-illuminated CCD) [1,2]. Optical etaloning is presented as the constructive and destructive interference patterns. The removal procedure is named as fringing suppression or defringing. There were many approaches developed by the researchers in the fields of astronomy, instrumentation and spectroscopy etc. [3–10]. Malamuth and Walsh both had used the fringe modeling method. They calculated the resulting fringe amplitude based on the known construction of CCD and reduced from the CCD images [3,4]. Howell has proposed a method which used a neon lamp as a flat field source and produces high SNR fringe frames to use for defringing an image during the calibration process [5]. Lagerholm had proposed an empirical method for the removal of the fringing in the spectral domain and the intensity variations in the imaging domain to improve the derived results from VIMOS-IFU data [6,7]. Using knowledge of the pattern, an automatic fringe removal method to the EFOSC images was proposed by Colin [8]. The etaloning is difficult to eliminate by algorithmic methods. There are some correction algorithms which allow removing unwanted fringes, but they work only under strictly controlled measurement conditions [9,10]. To a certain wavelength, the location of fringe determined by changes in the thickness of

* Corresponding author.
E-mail address: 871724220@qq.com (J. Jiang).

https://doi.org/10.1016/j.ijleo.2017.11.156
0030-4026/

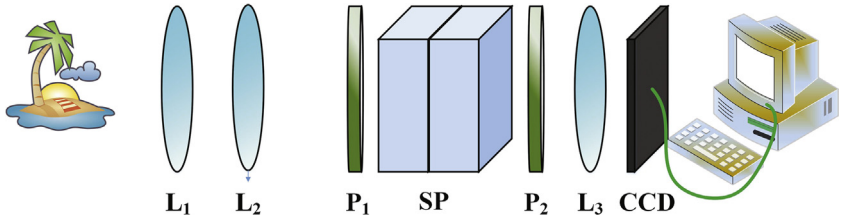

Fig. 1. The schematic of IISP.

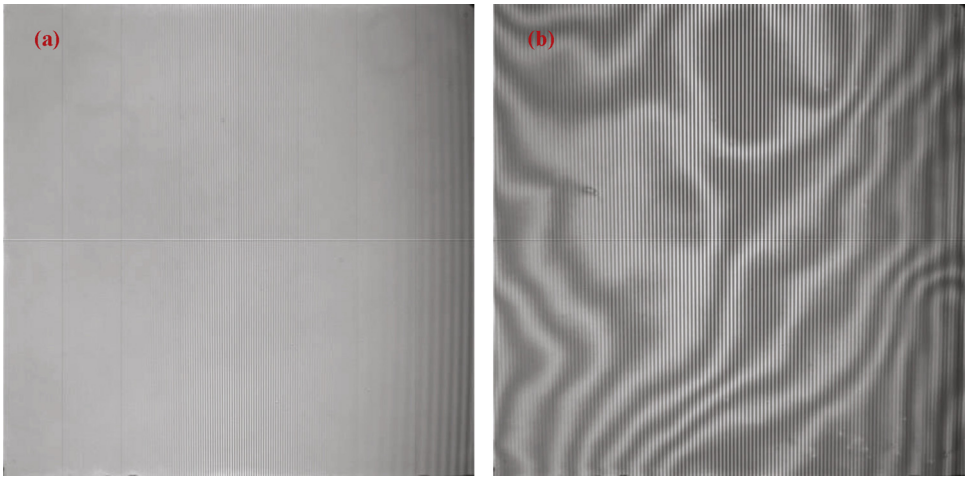

Fig. 2. The monochromatic interferograms at the wavelengths of 600 nm (a) and 900 nm (b).

the CCD is stable with time. The proposed methods are featured as requiring time-consuming operation, careful manual adjustments, preparation the construction of CCD, preparation the knowledge of fringe, or additional experiments such as the field flattening. Thereby, it is difficult to use these methods to implement defringing readily.

In the field of Fourier transform spectroscopy (FTS), the optical etaloning will occur while a monochromatic interferogram generated by the incident with a wavelength larger than 700 nm and detected by a back-illuminated CCD [11]. Its a challenging work to retrieve the precise spectral and spatial information since the fringe and interferogram generated with spectrometer are mixed with each other. In addition, the data processing such as the spectral wavelength and radiation calibration becomes much more difficult. The spectroscoptists were familiar with the traditional complex defringing methods based on the field flattening [12,13].

2. Interference imaging spectrometer

Interference imaging spectrometer (IISP) based on Savart polariscope (SP) is a system proposed by Zhang et al. to acquire the spatial and spectral information of the target simultaneously [14]. As shown in Fig. 1, a collimating lens is composed by the lenses L_1 and L_2; P_1 is the polarizer; SP is used as a beamsplitter to split the incident into two rays whose polarization orientations are perpendicular to each other; P_1 is the analyzer; L_3 is the imaging lens; a back-illuminated Sarnoff CCD is placed in the focal plane of L_3; the computer is used to data storage and processing. The spatial information can be obtained via realigning the data cube [15]. The spectral information should be retrieved from the realigned interferogram data cube by the fast Fourier transform or other approaches [16]. As shown in Fig. 1, a data cube with the spatial and spectral information could obtained after the data processing. The raw data taken by IISP is the superstition of the image can be taken by the traditional camera and the interferogram can be taken by the traditional Fourier transform spectrometer [15,16]. That is, the spatial and spectral information both are coded in the raw data. IISP is the combination of the traditional camera and Fourier transform spectrometer.

Calibration is an essential procedure during the data processing and information retrieval. In the wavelength, spectral response, and spectral resolution calibration process, the monochromatic interferograms are introduced. In the calibration of IISP, the etaloning occurred while the wavelength is larger than 700 nm. Fig. 2 shows two interferograms generated by the monochromatic lights at the wavelengths of 600 and 900 nm, respectively. It is obvious that the interferogram shown in Fig. 2(b) was seriously contaminate by the fringe introduced by the etaloning effects. However, the interferogram shown in Fig. 2(a) was pure. The vertical and horizontal stripes introduced by the CCD mosaic [17], obviously can be identified in Fig. 2(a).

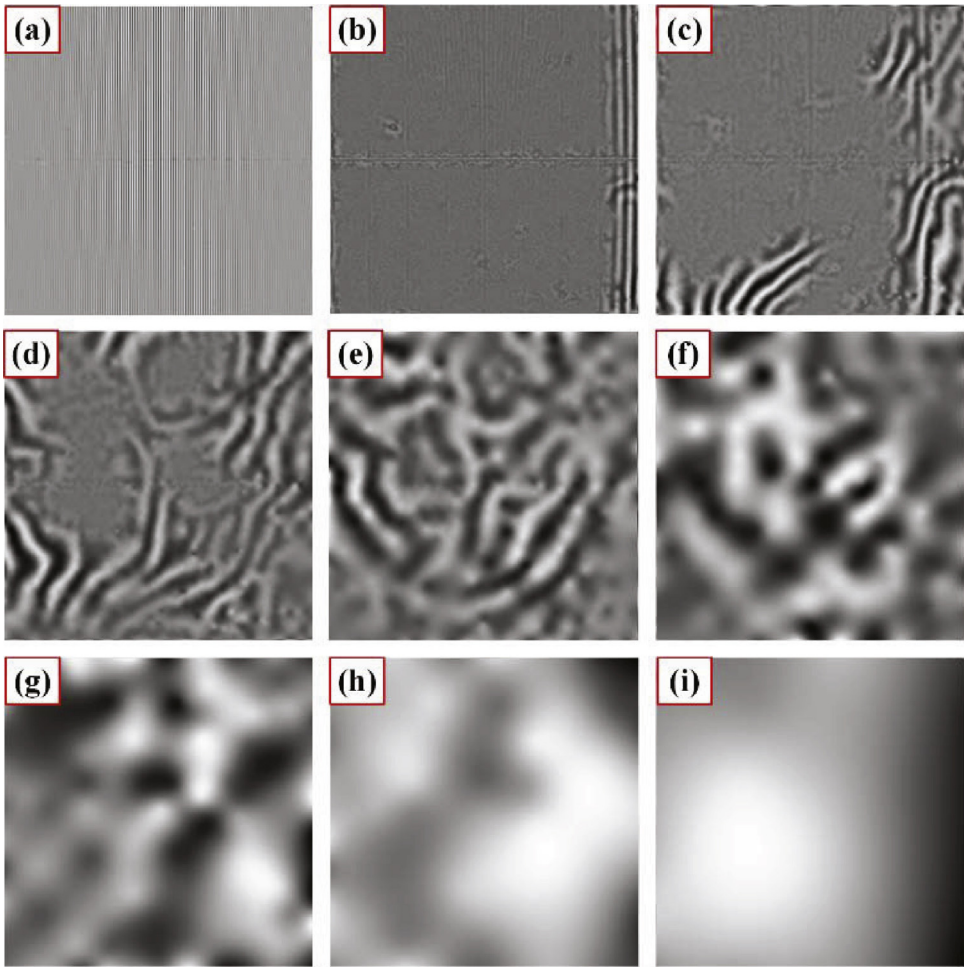

Fig. 3. The 9 BIMFs of contaminated interferogram were shown in Figs. 3(a)–(i).

Generally, the previous proposed methods such as field flattening were utilized to suppress the etaloning. It cannot be readily completed since they are time-consuming, requiring preparation of construction or knowledge of CCD, requiring extra device such as a neon lamp etc. Before the 21st century, its hard for us to suppress the etaloning with algorithm since the fringe is featured as nonlinear and stable with location at a certain wavelength and there was no effective algorithm for nonlinear signal processing. Empirical mode decomposition is a powerful tool developed by Huang for the nonlinear signal processing [18]. The bi-dimensional empirical mode decomposition (BEMD), a new form of multi-scale structure proposed by Nunes [19], is the two-dimensional extension of EMD. In this paper, an adaptive defringing method based on BEMD and PCA was developed for defringing in IISP.

3. BEMD and PCA based defringing

BEMD was successfully utilized in the fields such as image compression [20], image texture classification [21], image de-noising [22], image texture segmentation [23], texture synthesis [24], and image feature extraction [25] etc. The BEMD can be expressed as

$$I(m, n) = \sum_{i=1}^{L} Bimf_i(m, n) \tag{1}$$

where $I(m, n)$ is the raw image, is $Bimf$ the bi-dimensional intrinsic mode function (BIMF); the Lth BIMF, $Bimf_L$, is the residual $R(m, n)$. The BIMF with the smaller index corresponds to the higher frequency component, and $R(m, n)$ corresponds to the lowest frequency component [26]. $I(m, n)$ can be decomposed into L BIMFs (including the residual). The monochromatic interferogram and fringe, respectively, correspond to the high and low frequency information coded in the raw interferogram. The high and low frequency information can be extracted by the principal component analysis (PCA) method.

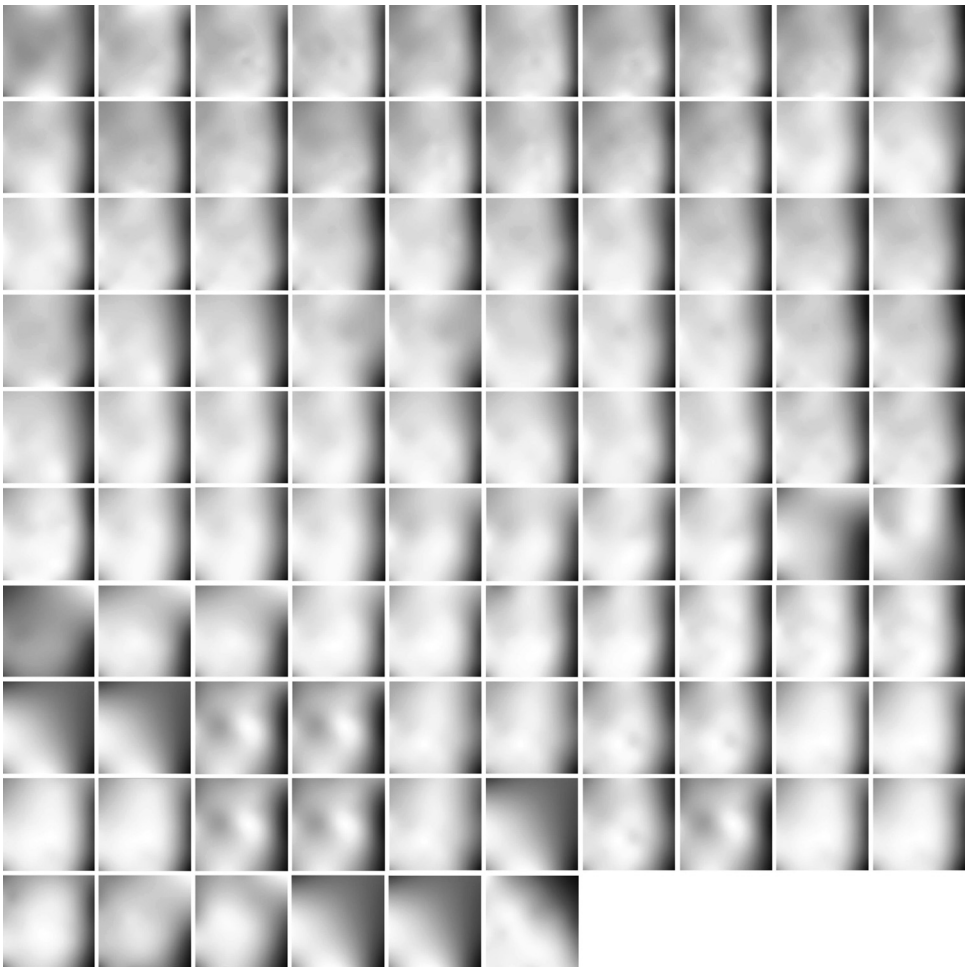

Fig. 4. The 9th BIMFs of the 96 monochromatic interferograms.

PCA is a powerful dimension reduction technique, which transforms the original data into the feature vectors of smaller dimensionality where the variance of the feature data is maximal [27]. It is the optimal linear scheme for reducing a set of high dimensional vectors into a set of lower dimensional vectors. The contaminated image is decomposed into different features corresponding to the various scales and frequencies [28]. As the most important information coded in the contaminated interferogram, the interferogram can be reconstructed by keeping only the eigenvectors corresponding to the largest eigenvalues.

The interferogram and fringe reconstructions are implemented as the following steps:

(1) Organize each BIMF into a column vector $P_{(1)}$with dimension $M \times N$. The resulting matrix $P = [P_{(1)}, P_{(2)}, P_{(3)}, \ldots, P_{(L)}]$ is a matrix with $M \times N$ rows and N columns;
(2) Compute the eigenvectors $V = [V_1, V_2, V_3, \cdots, V_L]$ and eigenvalue $\lambda = [\lambda_1, \lambda_2, \lambda_3, \cdots, \lambda_L]$ via PCA and sort them by decreasing eigenvalue;
(3) To represent the data with lower-dimensional vectors, the eigenvectors with the κ largest eigenvalues are computed. If β denotes the approximation precision of the κ largest eigenvectors, then the following relation holds:

$$R_c(\kappa) = \frac{\sum_{i=1}^{\kappa} \lambda_i}{\sum_{i=1}^{L} \lambda_i} \geq \beta. \tag{2}$$

(4) The corrected interferogram $I_{Rec}(m, n)$ and fringe $I_{Fre}(m, n)$ are given by

$$I_{Rec}(m, n) = P\Phi_1\Psi_1, I_{Fre}(m, n) = P\Phi_2\Psi_2 \tag{3}$$

where $Phi_1 = [V_1, V_2, V_3, \ldots, V_\kappa$, $Phi_1 = [V_{\kappa+1}, V_{\kappa+2}, V_{\kappa+3}, \ldots, V_L$, $\Psi_1 = [\lambda_1, \lambda_2, \lambda_3, \ldots, \lambda_\kappa]^T$ and $\Psi_2 = [\lambda_{\kappa+1}, \lambda_{\kappa+2}, \lambda_{\kappa+3}, \ldots, \lambda_L]^T$.

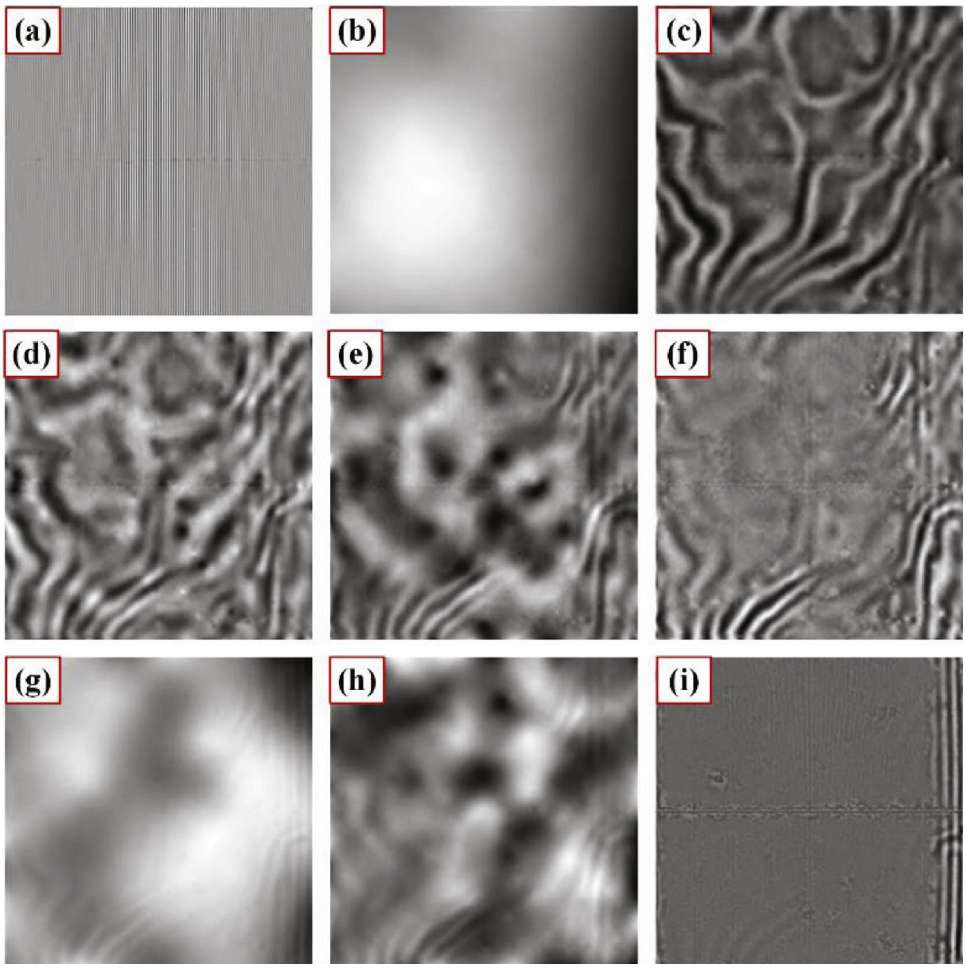

Fig. 5. The principal components taken by PCA.

4. Experiment

Fig. 3 shows the 9 BIMFs obtained by decomposing the contaminated interferogram shown in Fig. 2(b) via BEMD. It can be found that the interferogram information mostly is coded in the first IMF. There are a horizontal stripes located in the centre of the 1st to 4th BIMFs and 7 vertical stripes partially located in the 2nd and 3rd BIMFs. The fringe information is distributed over the 2nd to 8th BIMFs. The 9th BIMF can be considered as the non-uniformity of light field. In order to verify this hypothesis, 96 monochromatic interferograms obtained for spectral calibration were decomposed into 9 BIMFs. The wavelength range is 485–960 nm. The wavelength interval is 5 nm. The 9th BIMFs corresponding to the 96 interferograms are shown in Fig. 4. It can be found that they are very similar to each other. In the calibration procedure, the optical system and light field is stable. Thereby, it can be inferred that the 9th BIMF described the distribution of the non-uniform light field.

The 9 BIMFs shown in Fig. 3 were analyzed by PCA and the eigenvectors sorted by decreasing eigenvalues. The sorted principal components (PC) were shown in Fig. 5. The first BIMF corresponds to the first PC with the largest eigenvalue and highest frequency. The non-uniformity of light field represented by the last BIMF is sorted as the 2nd PC. The etaloning fringe information is described by the 3rd to 9th PCs. Each PC corresponds to a certain BIMF shown in Fig. 3. For instance, the 3rd PC corresponds to the 4th BIMF. By contrast, the 2nd to 9th PCs are evidently different to their corresponding BIMFs in the aspects of detail. The fringe information described by the PCs is much clearer.

In order to determine the threshold index κ in Eq. (2), the approximation precision of the largest eigenvectors, the stem plot of $R_c(\kappa)$ is shown in Fig. 6. κ is 1 if β equals to 60%, the interferogram is just reconstructed by first PC, and the fringe is reconstructed by the 2nd to 9th PCs. Both the non-uniformity of light field and etaloning fringe are considered as the fringe. If β is set as 80%, κ is 2, both the interferogram and non-uniformity are seemed as the interferogram. Given $\kappa = 1$ and $\kappa = 2$, respectively, the interferograms and fringes were obtained according to Eq. (3) and shown in Fig. 7. The fringe is mostly suppressed in the interferogram shown in Fig. 7(a). There is still some fringe information residue in the right part of the interferogram shown in Fig. 7(c). The horizontal stripe is not effectively suppressed in both of them. The stripes are

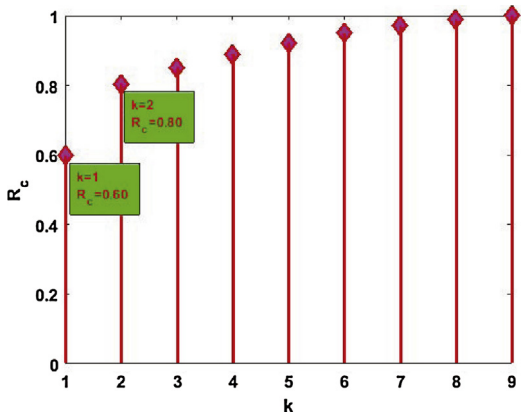

Fig. 6. The approximation precision of the κ largest eigenvectors.

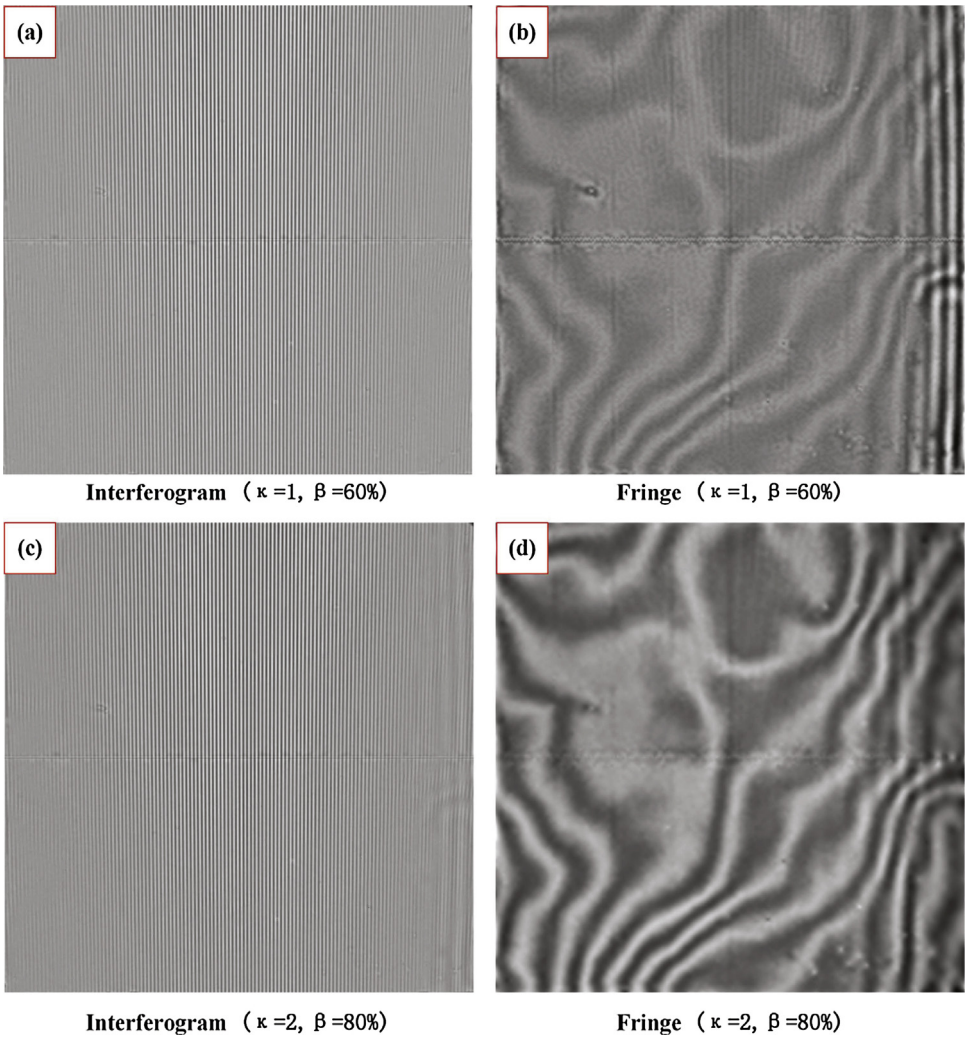

Fig. 7. The reconstructed interferograms and fringes with different κ and β.

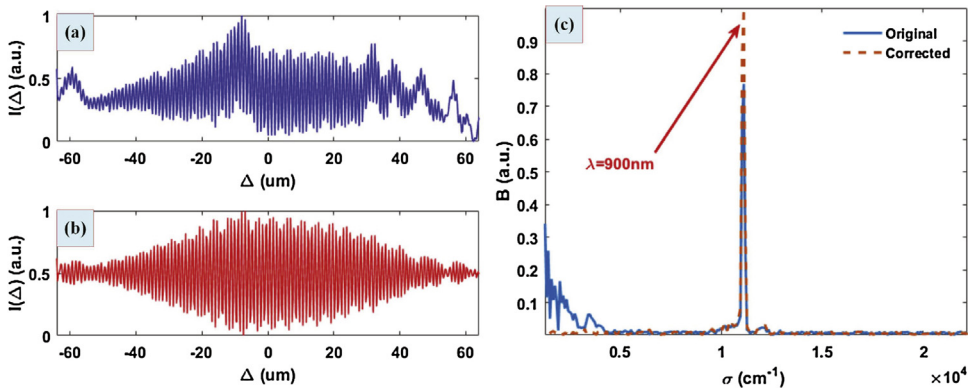

Fig. 8. The 1D contaminated (a) and corrected (b) interferograms and spectrums (c).

obviously found in the fringes shown in Figs. 7(b) and (d). Thereby, it is a better choice for us to set β as 60% and reconstruct the interferogram only by the 1st PC.

According to FTS, the spectrum $B(\sigma)$ can be retrieved by [29]

$$B(\sigma) = IFT\{I(\Delta)\}, \tag{4}$$

where σ the wavenumber, Δ is the optical path difference, *IFT* is the inverse Fourier transform, $I(\Delta)$ is an onedimensional (1D) interferogram.

The 100th row of the contaminated interferogram is depicted in Fig. 8(a). It can be found that the interferogram is modulated by a nonlinear background introduced by the fringing. A distorted spectrum was retrieved via inverse fast Fourier transform (IFFT) and shown in Fig. 8(c). It can be found that there are some sidelobes which are located in the small wavenumber region. The sidelobes are introduced by the nonlinear background of the interferogram. To suppress the sidelobes, the interferogram background removal must be implemented generally [26]. Fig. 8(b) shows the 100th row of the corrected interferogram shown in Fig. 7(a). As shown in Fig. 8(c), the spectrum in was obtained by IFT. Obviously, the nonlinear background and the sidelobes are suppressed effectively.

5. Conclusion

A nonlinear fringing suppression method based on BEMD and PCA was proposed for etaloning suppression in the Fourier transform spectrometer such as IISP. The raw interferogram with fringe was decomposed into L BIMFs firstly. The BIMFs were analyzed via PCA and all the PCs were sorted with their corresponding eigenvalues. A threshold based PCs synthesis method was proposed to reconstruct the interferogram and fringe. The feasibility of this approach was verified by the experiment. The best result was obtained while β was set as 60% and κ is 1. The interferogram was reconstructed by the 1st PC. The non-uniformity of the light field was described by the 2nd PC. The etaloning fringe was distributed over the 3rd to the last PCs. The vertical stripes sourcing from CCD mosaic were effectively suppressed simultaneously. The horizontal stripes were weakened to a certain degree. Comparing the 1D contaminated and corrected interferograms and spectrums, it was found that the nonlinear background of the interferogram and the sidelobes located in the small wavenumber region of the spectrum were suppressed effectively. Comparing with the previous proposed methods, it is an adaptive, time-saving, without prior knowledge, and automatic approach. It provides us an alternative method for the nonlinear fringing suppression in the fields of FTS, holographic imaging, and optical measurement and so on.

Acknowledgements

The work is supported by the National Natural Science Foundation of China under Grant Nos. 11504297, 61673314 and 11664004, Fundamental Research Funds for the Central Universities of China under Grant Nos. 2452015225, 2452017168, 2452017166, and 2452015226, Doctoral Scientific Research Foundation of Northwest A & F University under Grant Nos. Z109021504 and Z109021508, Science & Technology Co-ordination & Innovation Project of Shaanxi Province under Grant No. 2016 KTZDGY05-02, Opening fund of Guangxi Key Laboratory of Earth Surface Processes and Intelligent Simulation of Guangxi Teachers Education University under Grant No. 2015GXESPKF03, CSC Visiting Scholarship under Grant No. 201706305022.

References

[1] M.P. Lesser, CCD thinning, coating, and mounting research for astronomy, CCDs in Astronomy, Proceedings of the Conference, San Francisco, CA, Astronomical Society of the Pacific, 8 (1990) 65–75.
[2] S.B. Howell, Handbook of CCD Astronomy, 2nd ed., Cambridge University Press, Cambridge, 2006.

[3] E.M. Malumuth, R.S. Hill, T. Gull, B.E. Woodgate, C.W. Bowers, R.A. Kimble, D. Lindler, P. Plait, M. Blouke, Removing the fringes from space telescope imaging spectrograph slitless spectra, Publ. Astron. Soc. Pac. 115 (804) (2003) 218–234.
[4] J.R. Walsh, W. Freudling, N. Pirzkal, A. Pasquali, Modelling the Fringing of the ACS WFC and HRC Chips, ST-ECF Instrument Science Report ACS, 2003-012, 2003.
[5] S.B. Howell, Fringe science: defringing CCD images with neon lamp flat fields, Publ. Astron. Soc. Pac. 124 (913) (2012) 263–267.
[6] C. Lagerholm, H. Kuntschner, M. Cappellari, D. Krajnovic, R. Mcdermid, M. Rejkuba, A way to deal with the fringe-like pattern in VIMOS-IFU data, Astron. Astrophys. 541 (915) (2012) 515–518.
[7] C. Lagerholm, H. Kuntschner, M. Cappellari, D. Krajnovic, R. Mcdermid, M. Rejkuba, A method to deal with the fringe-like pattern in VIMOS-IFU data, Messenger 148 (2012) 17–19.
[8] S. Colin, C. Benoit, Automatic removal of fringes from EFOSC images, Telesc. Instrum. 152 (2013) 14–16.
[9] J. Fochesatto, J. Sloan, Spectral Sensing Research For Surface And Air Monitoring In Chemical, Biological And Radiological Defense and Security Applications, World Scientific, Singapore, 2009.
[10] R.L. McCreery, Raman Spectroscopy for Chemical Analysis, John Wiley & Sons, New York, 2000.
[11] N. Murakami, Calibration of the AKARI far-infrared imaging Fourier transform spectrometer, Publ. Astron. Soc. Jpn. 62 (5) (2010) 1155–1166.
[12] R. Wang, Z. Xu, Z. Jin, Z. Li, Y. Fu, Z. Liu, The first observation and data reduction of the multi-wavelength spectrometer on the new vacuum solar telescope, Res. Astron. Astrophys. 13 (13) (2013) 1240–1254.
[13] R. Casini, P.G. Judge, T.A. Schad, Removal of spectro-polarimetric fringes by two-dimensional pattern recognition, Astrophys. J. 756 (2) (2012) 828–842.
[14] C. Zhang, B. Xiangli, B. Zhao, Static polarization interference imaging spectrometer (SPIIS), Proc. SPIE 4087 (2000) 957–961.
[15] C. Zhang, X. Jian, Wide-spectrum reconstruction method for a birefringence interference imaging spectrometer, Opt. Lett. 35 (3) (2010) 366–368.
[16] W. Ren, C. Zhang, T. Mu, H. Dai, Spectrum reconstruction based on the constrained optimal linear inverse methods, Opt. Lett. 37 (13) (2012) 2580–2582.
[17] F. Valdes, IRAF data reduction software for the NOAO Mosaic, Astron. Data Anal. Softw. Syst. VI 125 (1997) 455–458.
[18] N.E. Huang, S.R. Long, Z. Shen, A new view of nonlinear water waves: the Hilbert spectrum, Annu. Rev. Fluid Mech. 31 (1) (1999) 417–457.
[19] J.C. Nunes, S. Guyot, E. Delechelle, Texture analysis based on local analysis of the bi-dimensional empirical mode decomposition, Mach. Vis. Appl. 16 (3) (2005) 177–188.
[20] A. Linderhed, 2D empirical mode decompositions in the spirit of image compression, Proc. SPIE 4738 (7) (2002) 1–8.
[21] Z. He, Q. Wang, Y. Shen, J. Jin, Y. Wang, Multivariate gray model-based BEMD for hyperspectral image classification, IEEE Trans. Instrum. Meas. 62 (5) (2013) 889–904.
[22] Y. Zhou, H. Li, Adaptive noise reduction method for DSPI fringes based on bi-dimensional ensemble empirical mode decomposition, Opt. Express 19 (19) (2011) 18207–18215.
[23] Z. Liu, P. Song, J. Zhang, J. Wang, Bi-dimensional empirical mode decomposition for the fusion of multispectral and panchromatic images, Int. J. Remote Sens. 28 (18) (2007) 4081–4093.
[24] Z.X. Liu, S.L. Peng, Boundary processing of bidimensional EMD using texture synthesis, IEEE Signal Process. Lett. 12 (1) (2005) 33–36.
[25] V.T. Tran, B.S. Yang, F. Gu, A. Ball, Thermal image enhancement using bi-dimensional empirical mode decomposition in combination with relevance vector machine for rotating machinery fault diagnosis, Mech. Syst. Signal Process. 38 (2) (2013) 601–614.
[26] C. Zhang, W. Ren, T. Mu, L. Fu, L. Jia, Empirical mode decomposition based background removal and de-noising in polarization interference imaging spectrometer, Opt. Express 21 (3) (2013) 2592–2605.
[27] J. Shlens, A tutorial on principal component analysis, Comput. Sci. 58 (3) (2014) 219–226.
[28] H. Yin, I. Hussain, Independent component analysis and non-Gaussianity for blind image deconvolution deblurring, Integr. Comput. Aided Eng. 15 (3) (2009) 219.
[29] J.M. Hollas, Modern Spectroscopy, 4th ed., John Wiley & Sons, New York, 2003.